PAPER

Check for updates

High coercivity $Pr_2Fe_{14}B$ magnetic nanoparticles by a mechanochemical method

Xiaoyun Shang,[a] Haoran Tu,[b] Jingjing Zhang, [ID] *[a] Bingying Ni,[a] Liying Wang, [ID] [a] Minggang Wang,[a] Chen Wu[a] and Zhankui Zhao*[a]

$Nd_2Fe_{14}B$ nanoparticles are widely used because of their outstanding hard magnetic properties. In fact, $Pr_2Fe_{14}B$ has higher magneto-crystalline anisotropy than $Nd_2Fe_{14}B$, which makes Pr-Fe-B a promising magnetic material. However, the chemical synthesis route to $Pr_2Fe_{14}B$ nanoparticles is challenging because of the higher reduction potential of Pr^{3+}, as well as the complex annealing conditions. In this work, $Pr_2Fe_{14}B$ nanoparticles were successfully synthesized *via* an efficient and green mechanochemical method consisting of high energy ball milling, annealing, and a washing process. Microstructural investigations revealed that the oxide precursors were uniformly wrapped by CaO and CaH_2, which formed an embedded structure after ball milling. Then, $Pr_2Fe_{14}B$ powder was synthesized *via* a time-saving annealing process. The impact of the Pr_2O_3 content and the preparation conditions was investigated. The coercivity of the as-annealed powder with 100 wt% Pr_2O_3 excess is 18.9 kOe. After magnetic alignment, the coercivity, remanence, and maximum energy product were: 9.8 kOe, 78.4 emu g^{-1}, and 9.8 MGOe, respectively. The present work provides a promising strategy for preparing anisotropic Pr-Fe-B permanent magnetic materials.

Introduction

Magnetic materials have been broadly applied in many industrial fields, including information storage, electronic devices, aerospace, energy generation, hybrid vehicles, wind power generators and so on.[1–3] Rare earth transition metal (RE-TM) permanent magnets, especially $Nd_2Fe_{14}B$, have gained considerable attention and are commonly applied because they are a high energy product.[4–6] The $Nd_2Fe_{14}B$ is one of the rare earth magnetic materials, found by Sagawa *et al.*[7] Because of the higher magneto-crystalline anisotropy of $Dy_2Fe_{14}B$ ($H_A = 158$ kOe) and $Tb_2Fe_{14}B$ ($H_A = 220$ kOe) compared to that of $Nd_2Fe_{14}B$ ($H_A = 67$ kOe),[3,8] partial substitution of Dy and Tb for Nd in Nd–Fe–B magnets has been proved to be a convenient method to raise coercivity (H_c).[7–11] However, the addition of Dy and Tb will decrease the magnetization and magnetic energy product due to the ferrimagnetic coupling between the rare earth atom and Fe and increases the cost due to the scarcity of Dy/Tb resources. Therefore, developing a high-coercivity $Nd_2Fe_{14}B$ magnetic material without Dy/Tb is becoming a hot topic in the permanent magnetic materials field. Compared to $Nd_2Fe_{14}B$, $Pr_2Fe_{14}B$ with a higher magneto-crystalline

anisotropy ($H_A = 87$ kOe) is a promising hard magnetic material with high coercivity.[12]

The majority of the research on the fabrication of the Nd–Fe–B magnets has centered on physical methods, including powder metallurgy sintering,[13] HDDR,[14] melt-spinning,[15,16] high-energy ball-milling,[17,18] and so on. Chemical methods, for example, microwave combustion,[3,21] sol–gel[19,20] and thermal decomposition have been applied in the preparation of $Nd_2Fe_{14}B$.[19] Compared with physical methods, a chemical method has distinct advantages in regulating size and morphology, which have a significant effect on the magnetic properties. The chemical synthesis used oxides as the precursors, which were reduction-diffused by CaH_2 or Ca to form $Nd_2Fe_{14}B$.[20–22] It is reported that the holding time during the annealing of the chemical synthesis method is generally greater than 90 min, which increased the energy loss and prolonged the production cycle so that limited the application in industrial production.[23–25] Recently, an efficient and green synthesis method, a mechanochemical method, has been used to synthesize $Nd_2Fe_{14}B$ magnetic nanoparticles.[26–30] The mechanistic method can promote the reaction between solids quickly and quantitatively, without adding solvent or adding only a nominal amount of solvent.

In this study, anisotropic $Pr_2Fe_{14}B$ magnetic powder with a high coercivity is synthesized by the simple mechanochemical method for the first time.[31–33] The reducing agent, CaH_2, was selected to reduce the Pr_2O_3, Fe_2O_3, and B_2O_3. The precursor samples were mixed uniformly and wrapped with CaH_2 after the high energy ball milling, which contributed to the completed

[a]College of Material Science and Engineering, Key Laboratory of Advanced Structural Materials, Ministry of Education, Changchun University of Technology, Changchun 130012, China. E-mail: zhangjj@ccut.edu.cn

[b]Key Laboratory of Physics and Technology for Advanced Batteries (Ministry of Education), Department of Physics, Jilin University, Changchun 130012, China

reduction of the as-milled oxide in the process of annealing. In this work, the optimal ball milling time, Pr_2O_3 content as well as annealing conditions were determined by comparing the magnetic properties. Meanwhile, the transition of the phases and microstructure were systematically investigated to reveal the reaction process.

Experimental

Materials

The precursors were commercially available and used without further purification: Pr_2O_3 (99.9%, Adamas-beta), and B_2O_3 (99.9%, Aladdin) powders, Fe_2O_3 (99.9%, Aladdin), and CaH_2 granules (99.9%, Aladdin), NH_4Cl (99.9%, Sigma-Aldrich), and methanol (99.99%, Sigma-Aldrich).

Synthesis

The fabrication process of the $Pr_2Fe_{14}B$ magnetic materials is demonstrated in Scheme 1. After milling for 2–5 h, the as-milled samples were annealed at 850 °C for 5 min in a glove box under an argon (Ar) atmosphere. The relative contents of Pr_2O_3, Fe_2O_3, B_2O_3 and were determined from the equation:

$$Pr_2O_3 + 7Fe_2O_3 + 0.5B_2O_3 + 25.5CaH_2 \rightarrow Pr_2Fe_{14}B + 25.5CaO + 25.5H_2\uparrow$$
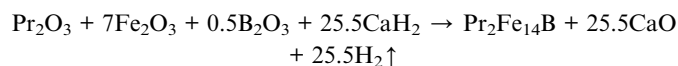
The CaH_2 acts as the reducing agent. The weight ratio of the preliminary reduction of Pr_2O_3 powders to CaH_2 was 1 : 1.5 to ensure full reduction. A portion of the mixture (2 g) was added to a stable steel vial under an Ar atmosphere. Because of the evaporation losses, an excess of 50 wt%, 100 wt% and 150 wt% Pr_2O_3 were added (denoted as $W_{50\%}$, $W_{100\%}$ and $W_{150\%}$). The ball milling was carried out using an 8000 M ball mill (SPEX Sample Prep) with a ball-to-powder ratio of 10 : 1, from 2 h to 5 h. The milling time was a key parameter and its influence on the phase transitions was investigated carefully. Subsequently the as-milled powders of 200 mg were annealed from room temperature to the target temperature in the RTP-1200 vacuum heating furnace. All the manipulations of the samples were performed in a LS800S glove box (Dellix, China) filled with a high purity Ar atmosphere. After agitating ultrasonically three times in a NH_4Cl/methanol solution, the annealed samples were cleaned for 10 min. The NH_4Cl/methanol solution was provided by dissolving 2 g of NH_4Cl in 100 ml of methanol. The NH_4Cl/methanol washing system was used, because CaO and NH_4Cl are able to react to generate NH_3 and $CaCl_2$ which dissolve clearly in methanol solution with very little heat generation.[26]

The sample components were determined by X-ray diffraction (XRD) on a D/max 2550 instrument (Rigaku) with Cu-Kα radiation. The elemental content and microstructure were determined using field emission scanning electron microscopy on a Supra 40/Gemini column instrument (Zeiss) with energy dispersive spectroscopy (EDS) detection and transmission electron microscopy (TEM) on a Talos F200S (FEI). The aligned sample was prepared as follows: the final powder was agitated ultrasonically in a methanol solvent and then placed in a 1 T magnetic field. After the methanol solvent had evaporated, the powder was solidified by addition of epoxy. Prior to magnetic measurement, a 9 T pulsed magnetic field was used to magnetize the sample to saturation. The final magnetic properties were measured by a vibrating sample magnetometer, VSM-7410 (VSM, Lake Shore Cryotronics) and the largest magnetic field was 2.8 T at 300 K.

The magnetization M and maximum energy product $(BH)_{max}$ of the powders were calculated using the density of a 100%-dense block material, and it was assumed that the magnets synthesized from the magnetic powders behaved similarly in the magnetic field. The sample density measured by the Archimedes principle was about 7.5 mg cm^{-1}.[32,34]

Results and discussion

The XRD patterns of the as-milled samples with different Pr_2O_3 contents are shown in Fig. 1(a)–(c). The Fe_2O_3 vanished and CaO, $Ca(OH)_2$ and α-Fe were observed, meaning that the Fe_2O_3 has been reduced to α-Fe by CaH_2. The Pr_2O_3 exists, especially in a sample with short milling time, suggesting that it is hard to reduce Pr_2O_3. The reduction potential of Fe_2O_3 and Pr_2O_3 were Fe^{3+}/Fe (−0.44 eV) and Pr^{3+}/Pr (−2.47 eV).[26,35] Therefore, Fe_2O_3 was reduced to α-Fe during high energy ball milling whereas Pr_2O_3 was seldom reduced. The $Ca(OH)_2$ is observed in Fig. 1(a)–(c). The formation of $Ca(OH)_2$ is due to the decomposition of CaH_2 being initially excessive, and it can easily convert into $Ca(OH)_2$ upon exposure to air.[36]

After annealing, the α-Fe and Pr_2O_3 phases gradually decreased and $Pr_2Fe_{14}B$ was observed (Fig. 1(d)–(f)), suggesting that the Pr_2O_3 was reduced during the annealing and then reacted with Fe and B to produce $Pr_2Fe_{14}B$. The B_2O_3 was reduced during the high energy ball milling, but it was difficult to observe in the XRD patterns due to the small amount. The reduction of Pr_2O_3 and the formation of $Pr_2Fe_{14}B$ were promoted by the ball milling. For $W_{50\%}$, the relative content of α-Fe increased abnormally when milled for 5 h, which should be
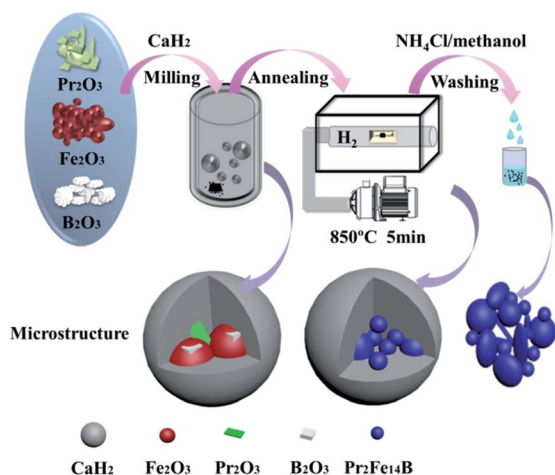
Scheme 1 A schematic diagram of the fabrication process of $Pr_2Fe_{14}B$-based nanoparticles and their microstructure.
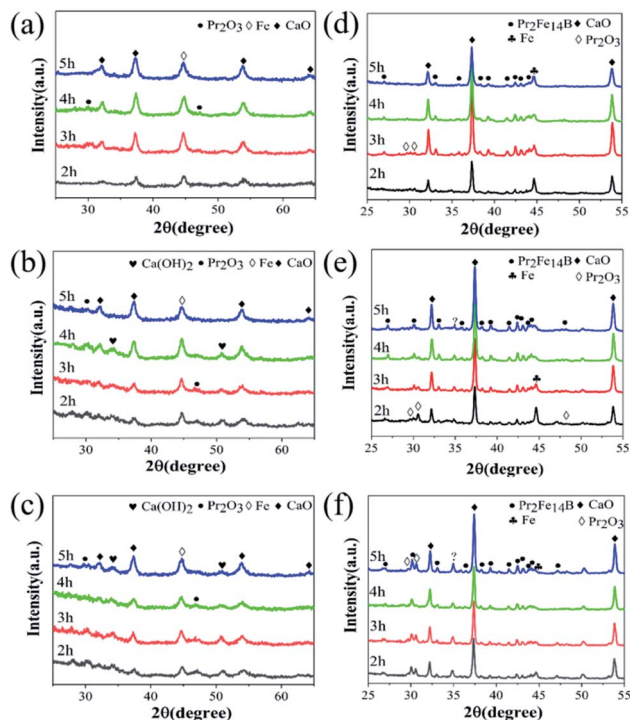
Fig. 1 The XRD diffraction patterns of samples with different amounts of Pr_2O_3 before annealing ((a) $W_{50\%}$, (b) $W_{100\%}$, (c) $W_{150\%}$) and after annealing ((d) $W_{50\%}$, (e) $W_{100\%}$, (f) $W_{150\%}$), all ball milled for 2–5 h.

attributed to the insufficiency of Pr_2O_3 and hence, the Pr content, caused by the loss of Pr during the long time of ball milling. No α-Fe appeared in the samples with more Pr_2O_3 ($W_{100\%}$ and $W_{150\%}$) and the long milling time, suggesting that the Pr_2O_3 content was sufficient.

The magnetization hysteresis loops of the as-milled powder (Fig. 2(a)) show the existence of abundant soft magnetic α-Fe phases, which is in agreement with the XRD results in Fig. 1(a). The VSM results in Fig. 2(a) show that the coercivity was about 500 Oe, which may be the reason for the existence of trace amounts of $Pr_2Fe_{14}B$ during the ball milling process.

The demagnetization curves of the as-annealed samples are presented in Fig. 3(a)–(c). With an increase of ball milling time, the permanent magnetic properties were first enhanced and
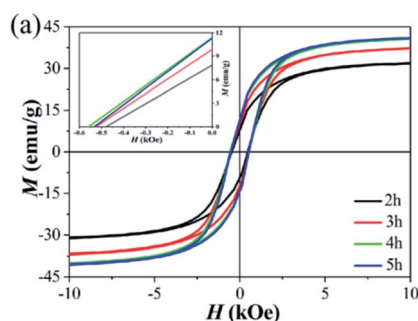

Fig. 2 Magnetization hysteresis loops of (a) an as-milled Pr_2O_3 sample ($W_{50\%}$). The inset shows the corresponding magnified second quadrant of these M–H curves.
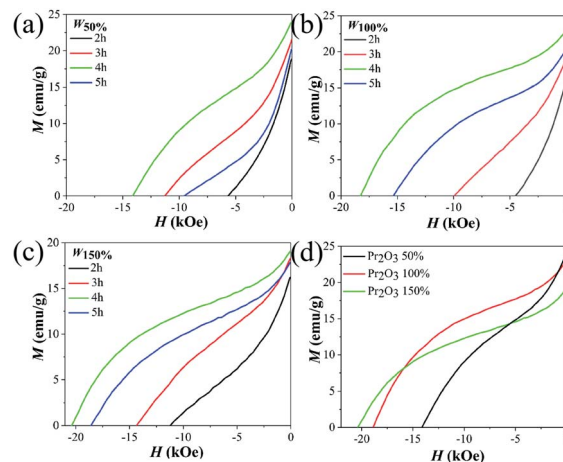

Fig. 3 Demagnetization curves of annealed Pr_2O_3 ((a) $W_{50\%}$, (b) $W_{100\%}$, (c) $W_{150\%}$), and the demagnetization curves of samples annealed at the optimum ball milling time of 4 h (d).

then weakened, the magnetism peaked at 4 h. The corresponding coercivity and remanence of the annealed samples ball milled for 4 h were 14.2 kOe and 24.1 emu g^{-1}, 18.9 kOe and 23.0 emu g^{-1}, 20.4 kOe and 19.2 emu g^{-1}, for $W_{50\%}$, $W_{100\%}$, and $W_{150\%}$, respectively, see Table 1.[37] The poor permanent magnetic properties of the samples with short ball milling time was because of the existence of magnetically soft α-Fe, as proved by the XRD patterns. Whereas excessive ball milling might result in a grain size which was too small, which decreased the coercivity by the superparamagnetic effect from the magnetic properties shown in Fig. 3(d) and Table 1, an insufficient Pr_2O_3 content caused the appearance of α-Fe which decreased the coercivity, and an excessive Pr_2O_3 content decreased magnetization because of the incomplete reduction of no magnetic Pr_2O_3. Therefore, the optimum Pr_2O_3 content is $W_{100\%}$, and the optimal ball milling time is 4 h.

The formation mechanism of $Pr_2Fe_{14}B$ in this mechanochemical method during annealing was further explored. The influence of the ball milling temperature was investigated based on Pr_2O_3 ($W_{100\%}$) ball milled for 4 h, as shown in Fig. 4. It was found that the diffraction peaks of $Pr_2Fe_{14}B$ become more obvious with the increase of the annealing temperature. Whereas magnetically soft α-Fe phase was found when the temperature rose to 900 °C, which may be due to the loss of Pr.

Table 1 The coercivity (H_c) and remanence (M_r) values of $Pr_2Fe_{14}B$ nanoparticles with different Pr_2O_3 levels

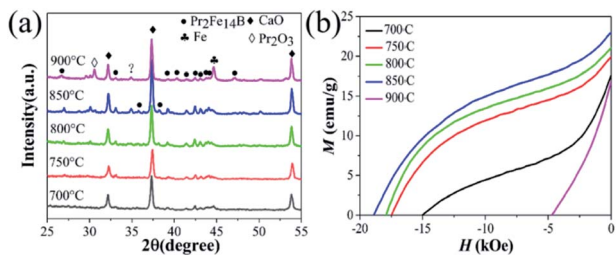| Sample name		Ball milling time			
		2 h	3 h	4 h	5 h
$W_{50\%}$	H_c (kOe)	5.6	11.2	14.2	9.6
	M_r (emu g^{-1})	18.7	21.5	24.1	20.1
$W_{100\%}$	H_c (kOe)	4.5	9.9	18.9	15.4
	M_r (emu g^{-1})	18.3	18.9	23.0	20.4
$W_{150\%}$	H_c (kOe)	11.2	14.3	20.4	18.6
	M_r (emu g^{-1})	16.3	18.3	19.2	17.9

Fig. 4 The XRD diffraction patterns (a) and demagnetization curves (b) of Pr_2O_3 ($W_{100\%}$) ball milled for 4 h and annealed at 700–900 °C.

The demagnetization curves (Fig. 4(b)) show that the optimum temperature was 850 °C, at which point the optimum permanent magnetic properties were gained. According to Fig. 5(a) and (b), the optimum holding time was 5 min. Extending the holding time has the same effect as raising the temperature.

The XRD patterns of samples, of different Pr_2O_3 contents, washed with NH_4Cl/methanol, with a ball milling time of 4 h are shown in Fig. 6(a). It can be observed that the $Pr_2Fe_{14}B$ phase is the major phase with a small amount of an unidentified phase. The magnetically soft α-Fe phase is observed in washed Pr_2O_3 ($W_{50\%}$). The standard data of PDF#50-0678 ($Pr_2Fe_{14}B$) is also presented. Comparing the washed Pr_2O_3 with PDF#50-0678, the peaks shifted a little to the lower 2θ positions, which arose from the formation of a small amount of $Pr_2Fe_{14}BH_x$ during the washing process. From the magnetic hysteresis curves (Fig. 6(b)), after removing CaO, the H_c of $W_{50\%}$, $W_{100\%}$ and $W_{150\%}$ with a ball milling time of 4 h decreased to 6.8 kOe, 9.4 kOe and 11.7 kOe, respectively. The obvious decrease of coercivity may be attributed to an occurrence of an exothermic oxidation reaction, which lead to a partial $Pr_2Fe_{14}B$ magnetic phase decomposition to soft magnetic phases. Accordingly, the magnetic properties of the final products were generally decreased, when the annealed samples were washed with an NH_4Cl/methanol solution to remove the CaO.[23,24,35,38–40] The M_r of Pr_2O_3 ($W_{50\%}$, $W_{100\%}$ and $W_{150\%}$) at a ball milling time of 4 h increased to 53.3 emu g^{-1}, 56.3 emu g^{-1} and 44.4 emu g^{-1} after the washing process, respectively, because of the elimination of nonmagnetic phases such as CaO, as well as $Ca(OH)_2$. The maximum energy product of Pr_2O_3 ($W_{50\%}$, $W_{100\%}$ and $W_{150\%}$) prepared at optimum conditions were 3.7 MGOe, 5.0 MGOe and 3.2 MGOe.
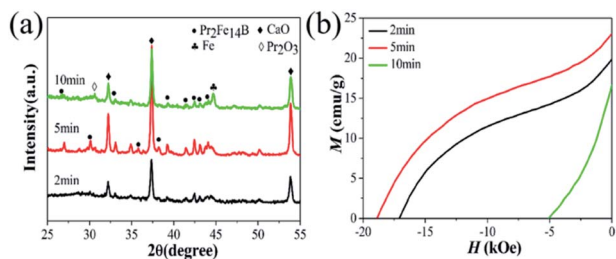

Fig. 6 The XRD diffraction patterns (a) and the magnetic hysteresis curves (b) of washed samples with different Pr_2O_3 levels after annealing.

Fig. 7 shows the hysteresis loops, parallel and perpendicular to the alignment direction, of magnetically aligned Pr_2O_3 ($W_{100\%}$). Two hysteresis loops show a distinct difference, meaning that the particle is a partial crystal and can be made into anisotropic magnets. With the original washed samples, the M_r value obviously increased, which demonstrated that most of the washed $Pr_2Fe_{14}B$ powders were single domain particles.[41] Fig. 7(b) shows the coercivities, remanence, saturation magnetization and maximum energy product of the magnetically aligned $Pr_2Fe_{14}B$ particles of $W_{50\%}$, $W_{100\%}$ and $W_{150\%}$. The M_r increased from 53.3 emu g^{-1}, 56.3 emu g^{-1}, 44.4 emu g^{-1} to 77.5 emu g^{-1}, 78.4 emu g^{-1}, 61.1 emu g^{-1}, after alignment, respectively. The best permanent magnetic property, a remanence of 78.4 emu g^{-1}, coercivity of 9.8 kOe, and a maximum energy product of 9.8 MGOe, was obtained in Pr_2O_3 ($W_{100\%}$).

To explore the microstructural evolution, SEM and TEM measurements were performed. It can be seen in Fig. 8(a), that the particles were relatively large after a ball milling time of 4 h. The TEM images (Fig. 9(a) and (b)) display sheet-shaped structures of $W_{100\%}$ after milling. Meanwhile, the HRTEM and HAADF images demonstrate that the as-milled powders have an embedded morphology, as shown in Fig. 9(c) and (d). The excessive amounts of CaH_2 ensure that the Pr_2O_3, α-Fe and B_2O_3 were uniformly wrapped by CaO or CaH_2 after high energy ball milling. This special structure may contribute to the fact that the reduction reaction happened in a short time. After annealing, the size of the particles did not change significantly, as

Fig. 5 The XRD diffraction patterns (a) and demagnetization curves (b) of Pr_2O_3 ($W_{100\%}$) milled for 4 h and then annealed to 850 °C and held for 2 to 10 min.
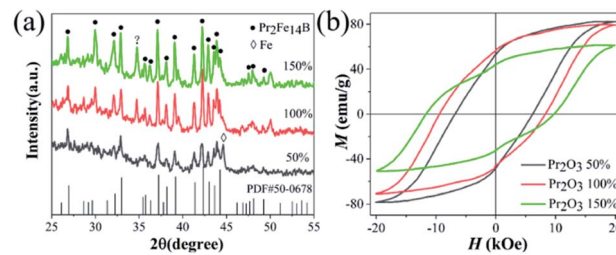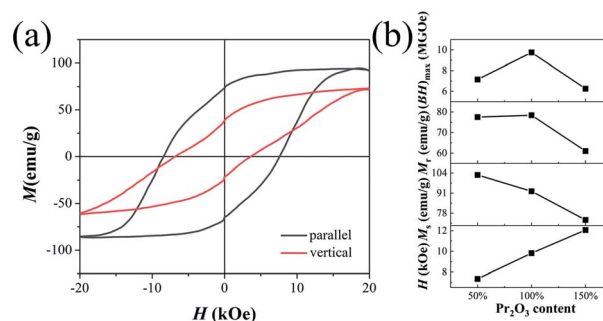

Fig. 7 The magnetization hysteresis loops of magnetically aligned Pr_2O_3 ($W_{100\%}$) (a), and H_c, M_s, M_r, and $(BH)_{max}$ data for aligned samples measured along the direction of alignment (b).
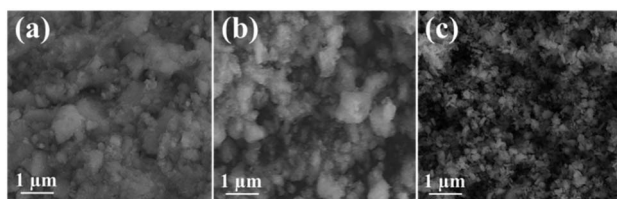
Fig. 8 SEM images of powder with a Pr_2O_3 content of $W_{100\%}$ ball milled for 4 h after (a) milling, (b) annealing, and (c) washing.
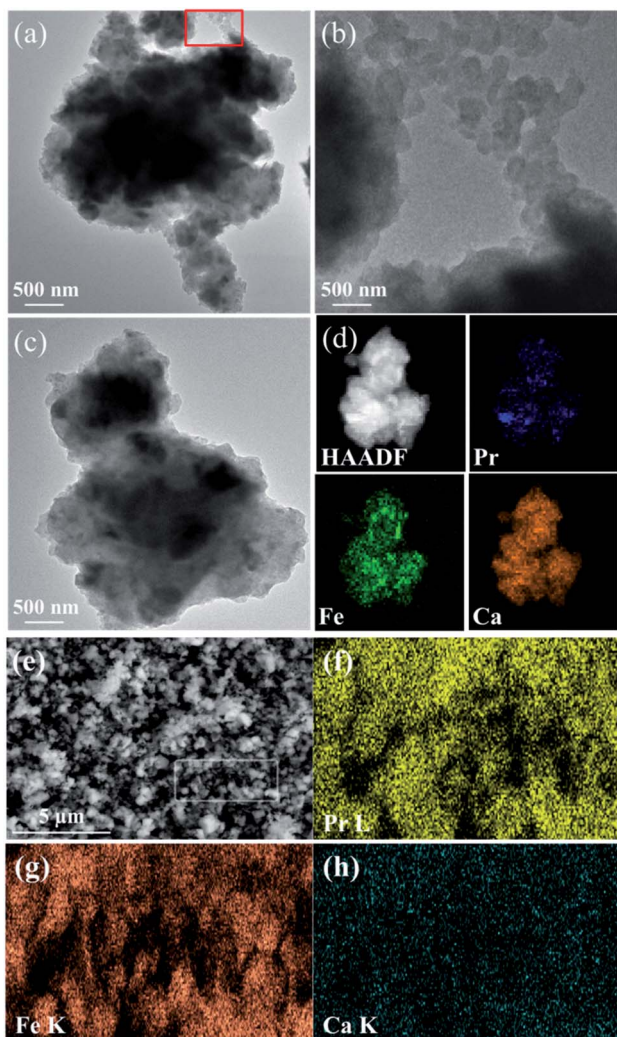

Fig. 9 The TEM (a) and HRTEM (c) images of Pr_2O_3 ($W_{100\%}$) powder after milling. (b) A magnified view of the red box in (a). (d) A HAADF image and elemental mapping of Pr, Fe, and Ca. (e) An SEM image of powder with $W_{100\%}$ after washing. The EDS element mapping of (f) Pr L, (g) Fe K, and (h) Ca K.

shown in Fig. 8(b), because of the covering of CaO on the $Pr_2Fe_{14}B$ particles. The existence of the CaO shell effectively inhibited the growth of the $Pr_2Fe_{14}B$ particles. After removal of the external CaO covering with a NH_4Cl/methanol solution, the irregular spherical or fine rod shaped particles with a smaller size were obtained, which is shown in Fig. 8(c).

Elements were uniformly distributed, as shown in Fig. 9(f) and (g) in the element mapping images. Due to the limitation of SEM, it was not possible to see the boron element. The atomic ratio between Pr and Fe was near to 0.21, which is similar to the best reactant ratio of Pr as well as the Fe precursors. The trace atomic ratio of Ca was 0.04% which means that the nonmagnetic phases as CaO and $Ca(OH)_2$ were eliminated in the cleaning process.

Conclusions

In summary, $Pr_2Fe_{14}B$ nanoparticles were prepared from Pr_2O_3, Fe_2O_3, B_2O_3, and CaH_2 powder *via* applying a mechanochemical method. The powders were partially reduced during high-energy ball milling, leading to the formation of a $Pr_2Fe_{14}B$ nucleus, which helped the as-milled powders to transform to $Pr_2Fe_{14}B$ in a time-saving annealing process. The phase compositions and magnetic properties can be enhanced *via* fine-tuning the Pr/Fe ratio and preparation conditions. Coercivity of 18.9 kOe was obtained in the sample with 100 wt% Pr_2O_3 excess, ball milled for 4 h and annealed to 850 °C for 5 min. After washing and magnetic alignment, the coercivity, remanence, and maximum energy product were improved to 9.8 kOe, 78.4 emu g^{-1}, and 9.8 MGOe, respectively. *Via* fine-tuning the particle size and microstructure, it is possible to further improve the magnetic performance of $Pr_2Fe_{14}B$ materials.

Conflicts of interest

There are no conflicts to declare.

References

1 X. Zhou, Y. L. Tian, H. Y. Yu, H. Zhang, X. C. Zhong and Z. W. Liu, *Waste Manag.*, 2019, **87**, 645–651.

2 H. Tu, Y. Yan, D. Cai, J. Wang, F. Li, F. Su and X. Du, *J. Magn. Magn. Mater.*, 2019, **490**, 165497.

3 X. Tan, H. Parmar, Y. Zhong, V. Chaudhary and R. V. Ramanujan, *J. Magn. Magn. Mater.*, 2019, **471**, 278–285.

4 D. B. D. Mooij and K. H. J. Buschow, *J. Less-Common Met.*, 1988, **142**, 349–357.

5 D. Goll, M. Seeger and H. Kronmüller, *J. Magn. Magn. Mater.*, 1998, **185**, 49–60.

6 N. Cannesan, J. M. Lebreton, A. J. Williams and I. R. Harris, *J. Magn. Magn Mater.*, 2002, **242**, 1372–1374.

7 M. Sagawa, S. Fujimura, N. Togawa, H. Yamamoto and Y. Matsuura, *J. Appl. Phys.*, 1984, **55**, 2083–2087.

8 S.-q. Hu, K. Peng and H. Chen, *J. Magn. Magn. Mater.*, 2017, **426**, 340–346.

9 M. Yue, X. Zhang and J. P. Liu, *Nanoscale*, 2017, **9**, 3674–3697.

10 D.-s. Wang, Z.-b. Li, F. Liu, Q. Ma, Y.-f. Li, Q. Zhao and X.-f. Zhang, *Mater. Lett.*, 2018, **228**, 509–512.

11 R. Goto, M. Matsuura, S. Sugimoto, N. Tezuka, Y. Une and M. Sagawa, *J. Appl. Phys.*, 2012, **111**, 2083.

12 W.-W. Yang, J. Luo, H.-J. Peng, Y.-L. Sui and X.-X. Gao, *Rare Met.*, 2014, **33**, 171–175.

13 J. Song, S. Guo, G. Ding, K. Chen, R. Chen, D. Lee and A. Yan, *J. Magn. Magn. Mater.*, 2019, **469**, 613–617.

14 J. J. Zhang, Y. Yan, H. M. Gao, H. M. Geng, X. Y. Feng, Z. P. Hou, H. D. Li, W. Q. Wang, F. Su and X. B. Du, *J. Magn. Magn. Mater.*, 2015, **374**, 317–320.

15 I. Shchetinin, P. Aggrey, I. Bordyuzhin, A. Savchenko, M. Gorshenkov, M. Zhelezniy, V. Menushenkov and P. Mogil'nikov, *Metals*, 2019, **9**, 497.

16 X. Lin, Y. Luo, H.-j. Peng, Y.-f. Yang, Y.-k. Dou, Z.-l. Wang, K.-s. Xu, S.-l. Diao and D.-b. Yu, *J. Magn. Magn. Mater.*, 2019, **490**, 165454.

17 Z. Wang, X. Liu, Z. Chen, R. Zhu, W. Yang, Z. Zhang, W. Wang, Q. Wu, K. M. U. Rehman and M. Shezad, *J. Supercond. Novel Magn.*, 2018, **32**, 715–720.

18 B. Z. Cui, W. F. Li and G. C. Hadjipanayis, *Acta Mater.*, 2011, **59**, 563–571.

19 L. Yu, C. Yang and Y. Hou, *Nanoscale*, 2014, **6**, 10638–10642.

20 H. Rahimi, A. Ghasemi, R. Mozaffarinia and M. Tavoosi, *J. Magn. Magn. Mater.*, 2017, **444**, 111–118.

21 L. Wu, A. Mendoza-Garcia, Q. Li and S. Sun, *Chem. Rev.*, 2016, **116**, 10473–10512.

22 Z. Ma, T. Zhang and C. Jiang, *Chem. Eng. J.*, 2015, **264**, 610–616.

23 P. K. Deheri, V. Swaminathan, S. D. Bhame, Z. Liu and R. V. Ramanujan, *Chem. Mater.*, 2010, **22**, 6509–6517.

24 C.-Q. Chen, D. Kim and C. Choi, *J. Magn. Magn. Mater.*, 2014, **355**, 180–183.

25 H. Rahimi, A. Ghasemi, R. Mozaffarinia and M. Tavoosi, *J. Magn. Magn. Mater.*, 2017, **424**, 199–206.

26 Y. Zhong, V. Chaudhary, X. Tan, H. Parmar and R. V. Ramanujan, *Nanoscale*, 2017, **9**, 18651–18660.

27 A. M. Gabay, X. C. Hu and G. C. Hadjipanayis, *J. Alloys Compd.*, 2013, **574**, 472–476.

28 A. Pal, A. Gabay and G. C. Hadjipanayis, *J. Alloys Compd.*, 2012, **543**, 31–33.

29 S. L. James, C. J. Adams, C. Bolm, D. Braga, P. Collier, T. Friscic, F. Grepioni, K. D. Harris, G. Hyett, W. Jones, A. Krebs, J. Mack, L. Maini, A. G. Orpen, I. P. Parkin, W. C. Shearouse, J. W. Steed and D. C. Waddell, *Chem. Soc. Rev.*, 2012, **41**, 413–447.

30 V. Chaudhary, Y. Zhong, H. Parmar, X. Tan and R. V. Ramanujan, *Chemphyschem*, 2018, **19**, 2370–2379.

31 K. Filipecka, P. Pawlik, A. Kozdraś, J. Filipecki and K. Pawlik, *Acta Phys. Pol., A*, 2019, **135**, 226–228.

32 P. Mingxiang, Z. Pengyue, G. Hongliang, Y. Hangfu and W. Qiong, *J. Magn. Magn. Mater.*, 2012, **324**, 2953–2957.

33 O. Koylu-Alkan, J. M. Barandiaran, D. Salazar, *et al.* Submicron $R_2Fe_{14}B$ particles, *AIP Adv.*, 2016, **6**(5), 056027.

34 H. Tu, Y. Yan, D. Cai, J. Wang, X. Shang, H. Tian, F. Su and X. Du, *Mater. Des.*, 2019, **183**, 108140.

35 H. X. Ma, C. W. Kim, D. S. Kim, J. H. Jeong, I. H. Kim and Y. S. Kang, *Nanoscale*, 2015, **7**, 8016–8022.

36 A. M. Gabay, X. C. Hu and G. C. Hadjipanayis, *J. Magn. Magn. Mater.*, 2014, **368**, 75–81.

37 W. F. Li, A. M. Gabay, X. C. Hu, C. Ni and G. C. Hadjipanayis, *J. Phys. Chem. C*, 2013, **117**, 10291–10295.

38 V. Swaminathan, P. K. Deheri, S. D. Bhame and R. V. Ramanujan, *Nanoscale*, 2013, **5**, 2718–2725.

39 J. H. Jeong, H. X. Ma, D. Kim, C. W. Kim, I. H. Kim, J. W. Ahn, D. S. Kim and Y. S. Kang, *New J. Chem.*, 2016, **40**, 10181–10186.

40 Y. Wang, J. Ahn, D. Kim, W. J. Ren, W. Liu, Z. D. Zhang and C. J. Choi, *J. Magn. Magn. Mater.*, 2017, **439**, 91–94.

41 C. Li, Q. Wu, Z. Ma, H. Xu, L. Cong and M. Yue, *J. Mater. Chem. C*, 2018, **6**, 8522–8527.